Journal of The Electrochemical Society, 2022 **169** 040552

Novel Method for Monitoring the Electrochemical Capacitance by In Situ Impedance Spectroscopy as Indicator for Particle Cracking of Nickel-Rich NCMs: Part III. Development of a Simplified Measurement Setup

Stefan Oswald,[1,=,*,z] Felix Riewald,[1,2,=] and Hubert A. Gasteiger[1,]**

[1]*Technical University of Munich, Chair of Technical Electrochemistry, Department of Chemistry and Catalysis Research Center, Garching, Germany*
[2]*BASF SE, New Battery Materials and Systems, Ludwigshafen, Germany*

As the optimization of the electrochemical performance of lithium-ion batteries by the adjustment of the composition of the cathode active materials (CAMs) has come to a limit, the focus has shifted to the modification of the morphological aspects. However, new methodologies for the quantification of characteristics such as particle size, particle cracking, and surface area change are needed. A previously reported impedance-based method allows for monitoring the capacitance of CAMs in the positive electrodes as indicator for their surface area but relies on a sophisticated cell setup. In this study, we deduce a stepwise simplification of the capacitance measurements from the setup using a gold-wire reference electrode to a conventional coin half-cell setup, which is commonly used in industry as testing platform for the initial benchmarking of newly developed CAMs. Additionally, it is shown that the CAM capacitance does not have to be extracted from a full impedance spectrum that requires an impedance analyzer, but that it can be obtained solely from a low-frequency single-point impedance measurement, which can be performed with a simple battery cycler. The working principle of this approach is validated using four different cell and electrochemical test hardware configurations (potentiostat, battery cycler) over several charge/discharge cycles.
 [DOI: 10.1149/1945-7111/ac67b3]

Manuscript submitted March 11, 2022; revised manuscript received April 10, 2022. Published May 12, 2022.

As many technical challenges of the 21st century center on cheap and efficient energy storage, the demand for lithium-ion batteries (LIBs) is not expected to stop soon. LIBs provide a good trade-off between energy and power density, efficiency, safety, and cost.[1–3] The limitation in energy density as well as the lion's share of cost (~50 %) of such a battery still lie in the cathode active material (CAM).[2–4] Currently, layered lithium transition metal oxides ($LiMO_2$) are the most widely used CAMs for transportation applications. For NCM ($Li_{1+\delta}Ni_xCo_yMn_zO_2$, $x+y+z+\delta = 1$, and $0 < \delta < 0.01$), a representative of commercially used CAMs, the transition metal ratio has been adjusted towards higher nickel contents, providing more specific capacity at a fixed cutoff potential, while decreasing the raw materials' cost due to the reduced cobalt content.[5,6]

However, the optimization of cell performance through the composition has come to a limit, as recent reports on newly developed and implemented CAMs with an ultra-high nickel content have repeatedly crossed the mark of 90 mol% nickel.[7–11] More innovative approaches pursue the modification of the particle morphology, which often include the tailoring of the primary crystallite size as well as of their shape and arrangement in secondary particle agglomerates.[12–16] This approach targets to diminish the various side reactions and degradation mechanisms that frequently scale with the CAM surface area, such as the electrochemical electrolyte oxidation at elevated potential (≥4.5 V_{Li}),[17] the chemical electrolyte oxidation by released lattice oxygen,[18–22] the formation of a resistive oxygen-depleted surface layer,[23–26] as well as the dissolution of transition metals (and their subsequent re-deposition on the anode).[27–31] Due to the anisotropic change of lattice parameters and the resulting change in unit cell volume upon (de)lithiation, mechanical fracture of the secondary particle structure occurs, leading to an increase of the interface area between CAM and electrolyte, which is therefore much higher during cell operation as compared to the pristine state.[25,32–36] The combination of these factors heavily influences the long-term cycling stability of actual cells.[14,26,37,38]

Therefore, the morphology and the accessible surface area has become a more and more important characteristic and descriptor for CAMs. So far, however, the morphological changes upon cycling are investigated mainly by means of post mortem analyses. For the analysis of cycled electrodes, typical approaches include the non-quantitative scanning electron microscopy and transmission electron microscopy of cross sections prepared by focused-ion beam milling (FIB-SEM/-TEM)[10,39–41] as well as the surface area determination via (Kr-)BET.[25,26,34,42] All of these are tedious and destructive, and a convenient tool for in situ CAM surface area tracking upon cycling is required.

Recently, a non-intrusive in situ impedance-based method has been reported, which monitors the CAM's capacitance as indicator for its electrochemically active surface area and can be directly included into the electrochemical cycling procedure.[34,36] However, this requires a rather sophisticated and intricate Swagelok T-cell setup with a micro-reference electrode (μ-RE; e.g., a gold-wire reference electrode (GWRE)[43]) as well as an impedance analyzer. Thus, it is not well suited neither for the use in an industrial setting (e.g., by CAM developers) nor for high-throughput screening, which is typically needed in material development.

In this study, we deduce a stepwise simplification of the capacitance measurements from a μ-RE setup to a conventional coin half-cell setup, which is the most used testing platform in industry for the benchmarking of new active materials. Additionally, it is shown that the capacitance does not have to be extracted from a full impedance spectrum provided by an impedance analyzer, but that it can be obtained solely from a low-frequency single-point impedance measurement, which can be performed with a conventional battery cycler without impedance capability.

Experimental

Electrode preparation.—For cell cycling, NCM electrodes were prepared from polycrystalline NCM851005 powder ($Li_{1.01}Ni_{0.85}Co_{0.10}Mn_{0.05}O_2$, 0.2 m^2_{BET}/g_{NCM} (determined by N_2-BET), BASF SE, Germany). To avoid contamination of the material by

[=]These authors contributed equally to this work.
*Electrochemical Society Student Member.
**Electrochemical Society Fellow.
[z]E-mail: Stefan.Oswald@tum.de

Table I. Overview of the four cell and test hardware configurations used for cell cycling studies of the NCM working electrodes, stating: the abbreviated label specifying a given configuration, the cell type, the type of counter electrode, how the impedance was measured and whether acquired as cell or as NCM cathode impedance, as well as the type of test hardware. Coin cells were assembled with 95 µl LP57 electrolyte and one glass fiber separator; T-cells with a µ-RE (GWRE) were assembled with 60 µl LP57 electrolyte and two glass fiber separators.

Label	Cell type	Counter electrode	Measured impedance	Test hardware
Z_{NCM}-LTO-B	T-cell w. µ-RE[43]	pre-lithiated LTO	NCM (spectrum)	Biologic
Z_{cell}-LTO-M	Coin cell	pre-lithiated LTO	cell (180 mHz point only)	Maccor
Z_{cell}-Li-B	Coin cell	lithium metal	cell (spectrum)	Biologic
Z_{cell}-Li-M	Coin cell	lithium metal	cell (180 mHz point only)	Maccor

moisture, all steps were performed in a dry room (at a room temperature of 20 °C and a dew point below −40 °C). The NCM powder was mixed at a mass ratio of 94:3:3 with conductive carbon (C65, carbon black SuperC65, 64 m^2_{BET}/g, TIMCAL, Switzerland) and polyvinylidene difluoride (PVDF, Solef5130, Solvay, Germany) as well as N-methyl-2-pyrrolidone (NMP, anhydrous, BASF SE, Germany) at a solid content of 61 wt% in a planetary centrifual mixer (ARE250, Thinky Corp., Japan). In a first step, C65, PVDF, and NMP were mixed for 30 min before the NCM powder was added and mixed for a subsequent 10 min.

The slurries were coated onto aluminum foil (20 µm, Nippon, Japan) with a box-type coater (wet-film-thickness: 100 µm, width: 6 cm, Erichsen, Germany) using an automatic coating table (5 mm/s, Coatmaster 510, Erichsen, Germany). All electrode sheets were then dried in a vacuum oven at 120 °C for 12 h before being calendered to a target value of 3.0 g_{NCM}/cm^3 (corresponding to an electrode thickness of 24 µm and a porosity of 32 %), using a laboratory calender (CA5, Sumet, Germany) with non-heated rolls (i.e., at room temperature) and a line pressure of 30 N/mm. Cathode working electrodes (WEs) with a diameter of 11 mm and 14 mm were punched out, having a loading of 7.5 ± 1.0 mg_{NCM}/cm^2_{WE} (the CAM loading of individual electrodes was determined with an accuracy of ±0.01 mg_{NCM}/cm^2_{WE}). For the counter electrodes, LTO ($Li_4Ti_5O_{12}$) electrodes with a diameter of 11 mm and 15 mm were punched out from commercially available LTO electrode sheets (LTO on aluminum, 3.5 mAh/cm^2, Custom Cells, Germany). All electrodes were vacuum-sealed and transferred without further exposure to air to an argon-filled glove box (<1 ppm O_2 and H_2O, Jacomex, Germany) where all cells were assembled.

Cell assembly.—In preparation of the cycling experiments, capacitively oversized LTO electrodes (3.5 mAh/cm^2, ∅ 11 mm for Swagelok T-cells and ∅ 15 mm for CR2032-type coin cells) were pre-lithiated in coin cells to a state of charge (SOC) of ∼10 %SOC, using a single glass fiber separator (∅ 17 mm, 675 µm nominal thickness, GF/D, VWR, Germany), 95 µl of LP57 electrolyte (1 M $LiPF_6$ in EC:EMC 3:7 w/w, <20 ppm H_2O, BASF SE, Germany), and a metallic lithium counter electrode (∅ 16 mm, 580 µm thickness, Gelon, China): after one full formation cycle at 30 mA/g_{NCM} between 1.2 V_{Li} and 2.0 V_{Li}, the LTO electrodes where lithiated to ∼10 %SOC at a specific current of 30 mA/g_{LTO} for 0.5 h. After pre-lithiation, the LTO electrodes were harvested from the cells and used as the counter electrode (CE) in the pseudo full-cells for the electrochemical cycling tests (note that pseudo full-cell here refers to a cell with a specific working electrode and a capacitively oversized, pre-lithiated LTO counter electrode). As it was discussed previously,[34] the use of a pre-lithiated, capacitively oversized LTO counter electrode provides: i) a stable half-cell potential of 1.55 V_{Li} over a wide SOC window; ii) a sufficiently large capacity to take up the lithium from the investigated NCM working electrodes; and, iii) an excess of lithium to compensate any lost lithium due to side reactions during cycling, thereby allowing to fully lithiate the working electrodes for the EIS measurements (i.e., for bringing the working electrodes into so-called blocking conditions).

For the electrochemical cycling tests with a µ-RE, spring-compressed Swagelok T-cells with capacitively oversized, pre-lithiated LTO as the counter electrode (∅ 11 mm) and NCM as working electrode (∅ 11 mm) were assembled using two glass fiber separators (∅ 11 mm, 240 µm nominal thickness, GF/A, VWR, Germany) and 60 µl of LP57 electrolyte. Between the two separators, a µ-RE was placed, namely a gold-wire reference electrode (GWRE) based on the setup described by Solchenbach et al.,[43] whereby the GWRE was lithiated in situ at 150 nA over 1 h from the LTO counter electrode before cycling (note that the GWRE lithiation charge of ∼0.15 µAh is negligible compared to the capacity of the counter electrode). This establishes a constant GWRE potential of 0.31 V_{Li}, which remains stable for more than 450 h. For details about the cell setup and the preparation of the gold wire, please refer to the original publication.[43]

For the electrochemical cycling tests without µ-RE, coin cells (CR2032, Hohsen Corp., Japan) with either capacitively oversized pre-lithiated LTO (∅ 15 mm) or lithium metal (∅ 16 mm) as counter electrode and NCM as working electrode (∅ 14 mm) were assembled using one GF/D type glass fiber separator and 95 µl of LP57 electrolyte. An overview of the configuration of the various cells with an NCM working electrode is displayed in Table I. In addition, symmetric coin cells using lithium metal (∅ 16 mm) for both electrodes were assembled using one glass fiber separator (∅ 17 mm, 240 µm nominal thickness, GF/A, VWR, Germany) and 95 µl of LP57 electrolyte, what allowed to determine the impedance of lithium metal electrodes upon stripping and plating during extended cell cycling. No pretreatment was carried out on the lithium metal surface before cell assembly.

Impedance spectroscopy.—All electrochemical impedance spectra (EIS) were included directly into the cycling procedure and recorded in a climate chamber (Binder, Germany) at 25 °C. For the experiments performed with a multi-channel potentiostat VMP3 (BioLogic, France), all spectra were recorded in potentiostatic mode (PEIS), with an amplitude of 15 mV for 8 points per decade from 100 kHz to 100 mHz, including a data point at a frequency of 180 mHz. This results in an acquisition time of ∼10 min per PEIS. For the T-cells, each EIS spectrum consists of a full-cell spectrum (between working and counter electrode) and, by using a GWRE, also of the half-cell spectrum (i.e., between the working and the micro-reference electrode). Note that measurements with the GWRE potentially contain artifacts at frequencies over 30 kHz;[44] however, as this work is focused on the low frequency region of the impedance spectra, in particular on the 180 mHz point, the impedance spectra obtained with the GWRE can be used without restrictions.

For the cycling experiments performed with a multi-channel battery cycler (Series 4000, Maccor, USA), the impedance was recorded for a single frequency point in galvanostatic mode (GEIS). For this purpose, an alternating current was simulated by applying a sine-like current-step function changing the current every 100 ms. Thus, the duration of a single sine-like current excitation was set to 5.6 s, resulting in a frequency of 178.56 mHz, which will be rounded to 180 mHz in the following for better readability. The current amplitude corresponded to a rate of *C*/50 (4 mA/g_{NCM}) for all battery cells. The sine-like current perturbation was repeated for 40 periods, resulting in a total duration of 224 s. The current perturbation and the voltage response of period 10 to 30 were fitted to a sine curve. The

resulting fitting parameters were then used to calculate the complex impedance.

For comparison of the impedance recorded with the potentiostat and with the battery cycler, three replicas each of a 1 mF electrolytic capacitor (±20 % tolerance, KEMET, USA) and a 10 mF supercapacitor (−20 %/+80 % Tolerance, KEMET, USA) were tested by PEIS using the Biologic potentiostat (by the parameters described above) as well as by a single-point GEIS measured at the Maccor battery cycler at a frequency of 180 mHz. For the latter, the current amplitudes were set to 0.02 mA (1 mF) and to 0.2 mA (10 mF), respectively. Before each measurement, the capacitors were left to rest in the climate chamber for at least 2 h for temperature equilibration.

Cell testing.—All electrochemical cycling tests were performed in a climate chamber (Binder, Germany) at 25 °C, using either a multi-channel potentiostat with full EIS capabilities (VMP3, Biologic, France) or a multi-channel battery cycler without integrated impedance capabilities (Series 4000, Maccor, USA), applying similar charge/discharge procedures. When using T-cells with a μ-RE, the GWRE was lithiated using the pre-lithiated, capacitively oversized LTO counter electrode (see above) prior to starting any cycling procedures. Throughout this study, voltages are given either in terms of the cell voltage in case of NCM/Li and Li/Li cells (labeled as V_{Li}) or, in the case of NCM/LTO cells, as cell voltage corrected for the potential difference between the LTO electrode and a lithium metal electrode ($V_{Li} \equiv V_{NCM/LTO} + 1.55$ V).

To acquire EIS spectra under so-called *blocking conditions*, represented by a semi-infinite charge-transfer resistance, the NCM working electrode is cycled to the fully discharged state at a potential of 2.55 V_{Li}, i.e., to nearly full lithiation (that this results in blocking conditions is shown in a previous study[34]).

The long-term cycling procedure (shown exemplarily in Fig. 4a for the first few cycles of Z_{cell}-Li-M, using lithium as counter electrode and cycled at the Maccor battery cycler, see Table I) was initiated by an open circuit voltage (OCV) phase of 2 h. To identify the *pristine* value of the NCM electrode capacitance, the NCM working electrode was discharged at *C*/10 (≡20 mA/g_{NCM} or ∼0.15 mA/cm^2_{WE}) from OCV to the lower cutoff potential of 2.55 V_{Li} (shown as the first step from OCV to "pristine" in Fig. 4a), where a constant voltage (CV) hold was performed (referred to as CCCV mode, always with either a 1 h CV hold when using the Biologic potentiostat or until the current dropped below *C*/250 when using the Maccor battery cycler), followed by an EIS. During *conditioning* (shown as the steps from "pristine" over point A to point B in Fig. 4a), the electrodes were charged at *C*/10 in constant current (CC) mode for 1 h, then discharged to the lower cutoff potential of 2.55 V_{Li} at *C*/10 in CC mode, where again a CV hold of 1 h (Biologic) or until the current dropped below *C*/250 (Maccor) was performed (shown as the step from point B to #0 in Fig. 4a), followed by an EIS (point #0 for cycle 0). Since nickel-rich CAMs are commonly slightly overlithiated (by up to 1 %) in the synthesis process, the conditioning step was included in the procedure to ensure comparable impedance spectra for each cycle, namely by assuring that similar SOCs are obtained by the potential hold at 2.55 V_{Li} (especially critical when comparing different NCM active materials). For the consecutive *formation*, three charge/discharge cycles are executed, with a charge to the upper cutoff potential of 4.3 V_{Li} at *C*/10 (in CC mode), and with a discharge to a lower cutoff potential of 2.55 V_{Li} at *C*/10 with a final CV hold before an EIS was recorded (marked by the #1 point in Fig. 4a for the first formation cycle, referred to as cycle 1). The formation was followed by an extended *cycling* procedure that consisted of five cycles per set: (i) cycling four times at 1*C* (≡200 mA/g_{NCM} or ∼1.5 mA/cm^2_{WE}) in CCCV mode (either for 30 min or until the current drops below *C*/10 at 4.3 V_{Li}) for charge and in CC mode to 3.0 V_{Li} for discharge; (ii) a fifth cycle performed at *C*/10, followed by a CV hold at 2.55 V_{Li} and an EIS (i.e., identical to the formation cycles). This set of five cycles was repeated for 65 charge/discharge cycles. The impedance spectra taken in blocking conditions are numbered by the number of full cycles that the electrodes had performed up to that point (e.g., #8 after three formation cycles and one set of five cycles).

A similar cycling procedure was applied for the symmetric lithium-lithium cells cycled with the Biologic potentiostat (shown in Fig. A·1): After an OCV period of 1 h and an initial PEIS at OCV in the pristine state, the cells were charged for 1 h and discharged for 1 h at a current of 0.30 mA (corresponding to 0.15 mA/cm^2_{Li} (similar to the areal current of 0.18 mA/cm^2_{WE} in the NCM cells), mimicking the conditioning step of the NCM cells (*C*/10) with lithium metal counter electrode), both charge and discharge followed by a rest step of 1 h and a PEIS. During three formation cycles, the cells were charged for 10 h and discharged for 10 h at a current of 0.30 mA, while both charge and discharge were completed by a 1 h OCV period and a PEIS. During cycling, the cells were charged for 1 h and discharged for 1 h, both at a current of 3.0 mA for four cycles (mimicking the cycling of the NCM cells at 1*C*) and at a current of 0.30 mA for a single charge/discharge cycle, whereby after each set of four cycles at 3.0 mA and one cycle of 0.30 mA, an OCV period of 1 h and a PEIS is added, similar to the formation cycles. This set of five cycles was repeated for 65 charge/discharge cycles. The impedance spectra are numbered by the number of full cycles that the cell had performed up to that point (e.g., #8 after three formation cycles and one set of five cycles).

Results and Discussion

Comparison of impedance contributions.—As proven in part I of this study,[34] the capacitance of the electrochemical double layer of the components of a battery electrode is proportional to their respective electrochemically active surface areas. To be able to extract the cathode electrode capacitance, it is required to increase the charge-transfer resistance to semi-infinite values (i.e., into blocking conditions). To achieve this, the NCM electrodes were fully lithiated, resulting in a capacitive branch of the electrode/electrolyte interface dominating the impedance spectra for medium to low frequencies (<100 Hz), a region in which contributions of other effects (e.g., of the pore resistance) are negligible.[45,46] Further, it was demonstrated that it is not necessary to extract the electrode capacitance from a fit of the impedance data by an equivalent circuit, but that it is possible to calculate the electrode capacitance *Q* from the imaginary impedance $\mathrm{Im}(\boldsymbol{Z}_{\omega_0})$ of a single frequency point at $\omega_0 = 180$ mHz using the following formula:[34]

$$Q \approx \frac{1}{\omega_0 \cdot (-\mathrm{Im}(\boldsymbol{Z}_{\omega_0}))} \qquad [1]$$

This approximation for the electrode capacitance is possible solely since, at this frequency of 180 mHz, the imaginary impedance of a constant-phase element (CPE) and, therefore, of the extracted capacitance does not vary significantly with the phase angle α (error of <1 % if $\alpha > 0.85$). As it was shown in part I of this study, frequencies in the range of 160 to 220 mHz are suitable to be used with Eq. 1, while the optimal value depends on the expected/determined values for the phase angle of the investigated electrode as well as on the desired accuracy.[34] In this study, the value of 180 mHz is used for better comparability with the previous reports.

The imaginary impedance of an NCM electrode with a loading of ∼10 mg/cm^2_{WE} at 180 mHz was reported to be on the order of $-\mathrm{Im}(\boldsymbol{Z}_{NCM}) = 700$–$1000\ \Omega \cdot cm^2_{WE}$ in the pristine state and on the order of $-\mathrm{Im}(\boldsymbol{Z}_{NCM}) = 200$-$300\ \Omega \cdot cm^2_{WE}$ after 200 cycles to 4.5 V_{Li} or after being cycled to high states of charge (SOCs),[34,35] depending on mass loading and electrode composition. In order to utilize this method in a cell configuration without reference electrode, where only the impedance of the entire cell can be determined instead of the individual electrode impedances that are accessible with a μ-RE, the relative contributions of the imaginary impedance of working

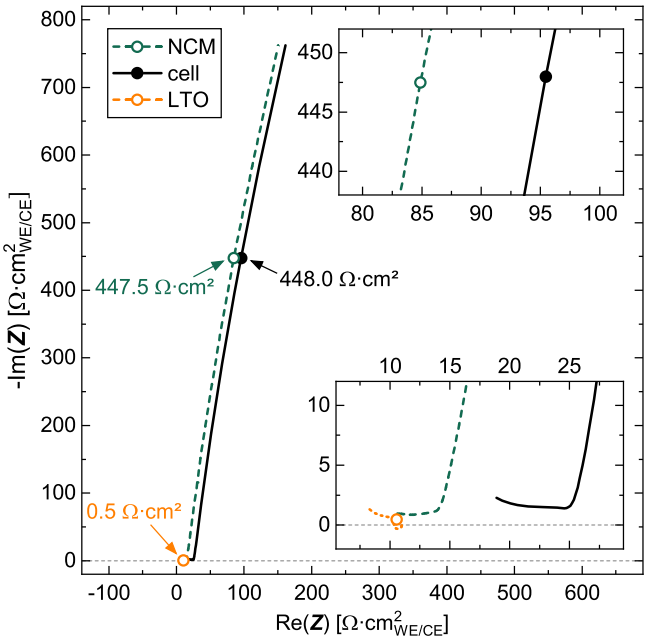

Figure 1. Nyquist plot of the impedance data acquired with the Z_{NCM}-LTO-B cell (see Table I) after the conditioning step (corresponding to cycle #0, following the procedure displayed in Fig. 4a), showing the impedance spectra of the NCM working electrode (dark green), of the capacitively oversized pre-lithiated LTO counter electrode (orange), as well as of the entire cell (black), all normalized to the geometrical surface area of the cell (0.94 $cm^2_{WE/CE}$). The frequency points at 180 mHz are indicated by circles and the respective values of the imaginary impedance are marked by the arrows. The insets magnify the region near the frequency point of 180 mHz for the cell and NCM impedance (upper panel) and for the LTO impedance (lower panel). Pseudo full-cells were assembled with 60 µl LP57, two glass fiber separators, and a µ-RE, and cycled at 25 °C. Impedance spectra were acquired between 100 kHz and 100 mHz (15 mV amplitude) with the NCM working electrode being in blocking conditions, achieved after a potential hold of 1 h at 2.55 V_{Li}.

and counter electrode need to be evaluated for the frequency point of 180 mHz.

Figure 1 shows the impedance spectra acquired with the Z_{NCM}-LTO-B cell (see Table I) at 2.55 V_{Li} for cycle #0 (after the conditioning step), presenting the impedance of the entire cell (black line) as well as the one of the individual contributions of the NCM (dashed dark green line) and the LTO electrode (dashed orange line). Both the cell impedance as well as the NCM impedance show a capacitive branch, whereby the cell impedance is mainly shifted to larger real impedance values by ~10 Ω·cm^2; the imaginary impedance at 180 mHz (marked by the circles in Fig. 1), however, is similar for both, namely -Im($\mathbf{Z}_{cell}$) = 448.0 Ω·$cm^2_{WE/CE}$ for the entire cell and -Im($\mathbf{Z}_{NCM}$) = 447.5 Ω·cm^2_{WE} for the NCM electrode only. The difference in the real as well as in the imaginary impedance is solely owed to the additional contribution of the LTO counter electrode, which at 180 mHz has impedance values of Re($\mathbf{Z}_{LTO}$) = 10.6 Ω·cm^2_{CE} and -Im($\mathbf{Z}_{LTO}$) = −0.5 Ω·cm^2_{CE}. The impedance loop observed for the impedance spectrum of the LTO counter electrode originates from the inherent difference of anode and cathode impedance of more than three orders of magnitude, which induces artifacts when utilizing a µ-RE.[47]

As the contribution of the LTO counter electrode is not altered significantly upon cycling (<0.1 Ω·cm^2_{CE} in imaginary direction and <0.5 Ω·cm^2_{CE} in real direction, data not shown), and as the negative imaginary impedance of the NCM working electrode at 180 mHz does not decrease below 200 Ω·cm^2_{WE} in all of the measurements presented in this study (as well as in the ones of part I and part II of this study), the relative contribution of the imaginary impedance of the LTO counter electrode in comparison to the one of the entire cell does not exceed 0.3 %. This finding allows for a reasonably accurate estimation of the capacitance of the NCM electrode from the impedance measurement of the entire cell, enabling the elimination of the µ-RE for the setup with an LTO counter electrode.

Since a full lithiation of the NCM active material is required to achieve blocking conditions for the NCM working electrode,[34] a lithium reservoir is needed in the counter electrode. Therefore, counter electrodes such as pre-lithiated graphite or LTO, pre-delithiated LFP, or even lithium metal might fulfill these prerequisites. However, the magnitude of their imaginary impedance value at 180 mHz needs to be sufficiently low to assure that their contribution to the total impedance of the entire cell is negligible. Due to the lithium loss upon solid-electrolyte interphase (SEI) formation, the use of pristine graphite is here therefore not possible.

Impedance of lithium metal.—As half-cells are easy to build and most used for the initial characterization of active materials, lithium metal is investigated as possible counter electrode for the capacitance measurements in a coin cell without reference electrode. To mimic the cycling procedure to which the lithium metal electrode is subjected in the later discussed NCM/Li cells, a similar protocol with corresponding areal currents is applied to the symmetric Li/Li cells. This procedure includes "*C*/10" cycles at 0.30 mA (≡ 0.15 mA/cm^2_{Li}) and "1*C*" cycles at 3.0 mA (≡ 1.5 mA/cm^2_{Li}), as it is depicted in Fig. A·1 (note that, even though no value for the cell capacity was assigned for the symmetric Li/Li cells, the *C*-rates in quotation marks refer to the corresponding *C*-rates that would be applied in an NCM/Li cell based on the mass loading of the NCM electrodes used in this study).

Figure 2 presents the impedance spectra of lithium metal cycled in a symmetric cell with LP57 electrolyte, divided by a factor of 2 to obtain the impedance of one electrode from the symmetric cell setup and normalized to the geometric surface area of one lithium metal electrode (2.0 cm^2_{Li}), resulting in the areal impedance of one lithium metal electrode only (including 50 % of the separator resistance). The spectrum of the pristine cell (black) shows a large semicircle at high to medium frequencies, with an apex of -Im($\mathbf{Z}$) = 60 Ω·cm^2_{Li} at 376 Hz, and a substantially smaller semicircle at low frequencies that is partially overlapped by the large semicircle; the large semicircle is typically attributed to the charge transfer through a compact SEI and the small semicircle potentially stems from the diffusion of lithium ions through a porous SEI.[48] The observed high-frequency resistance (HFR, measured at 100 kHz) of 10 Ω·cm^2_{Li} is due to the ohmic resistance of the electrolyte in the porous separator.[45] The frequency point at 180 mHz (marked by the empty circle) shows an imaginary impedance of -Im($\mathbf{Z}$) = 2.7 Ω·cm^2_{Li}.

After the conditioning step at 0.30 mA ("*C*/10") (dark blue, corresponding to cycle #0), the imaginary impedance contribution of the apex of the large semicircle has reduced in magnitude by 38 % to -Im($\mathbf{Z}$) = 37 Ω·cm^2_{Li}, what we assign to an increasing surface area of the lithium metal electrodes upon formation of dendrites and cavities.[48,49] This trend further continues during the repeated lithium stripping and plating of the subsequent cycles at 3.0 mA ("1*C*"). Up to cycle #8 (turquoise), the negative imaginary impedance maximum has already decreased to -Im($\mathbf{Z}$) = 4.4 Ω·cm^2_{Li}, whereas the HFR stays constant. Starting at cycle #28 (green), only one full semicircle is visible in the applied frequency range, whereas the onsets of two other ones appear at lower and higher frequency: for both cycle #28 and #48 (dark green), the visible semicircle shows a negative imaginary impedance maximum of -Im($\mathbf{Z}$) = 2.0 Ω·cm^2_{Li} and 2.2 Ω·cm^2_{Li}, respectively, which then increases to -Im($\mathbf{Z}$) = 8.6 Ω·cm^2_{Li} for cycle #68 (brown). The HFR, however, initially undergoes a slight increase (cycle #3: 10 Ω·cm^2_{Li}; #8: 11 Ω·cm^2_{Li}; #28: 20 Ω·cm^2_{Li}) but then starts to significantly rise in the following cycles (#48: 47 Ω·cm^2_{Li}; #68: 205 Ω·cm^2_{Li}).

This behavior is reflected in the lithium/lithium cell voltage extracted from the measured voltage profile shown in Fig. A·1, which, even though the applied currents are constant for the "1*C*" and "*C*/10" cycles, respectively, starts to increase drastically starting after cycle

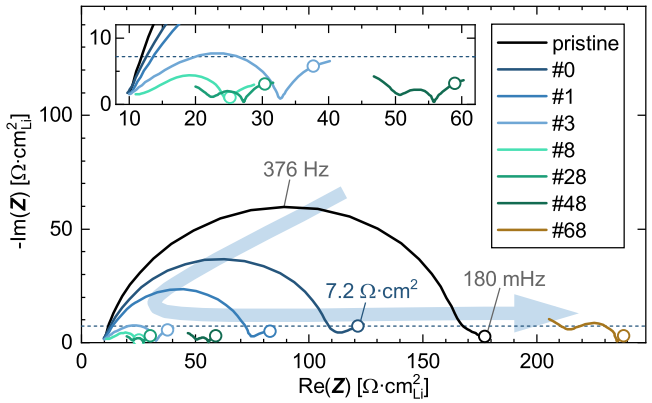

Figure 2. Nyquist plot of the impedance spectra of a symmetric lithium/lithium cell upon cycling at 25 °C (following the procedure displayed in Fig. A·1), whereby the impedance values were divided by a factor of 2 to obtain the value of one electrode only and were further normalized to the geometrical surface area of one lithium metal electrode (2.0 cm^2_{Li}). The frequency points at 180 mHz are indicated by empty circles, and the imaginary impedance of 7.2 Ω·cm^2 is marked by the horizontal dashed dark blue line. The inset magnifies the low-impedance region of the spectra between cycle #3 and #48. Coin cells were assembled with lithium metal as both electrodes, with 95 µl LP57 electrolyte, and one glass fiber separator.

#28: At "*C*/10" (≡ 0.30 mA or 0.15 mA/cm^2_{Li}), the cell voltage required to drive the applied current decreases during the three formation cycles from ∼0.05 V during the conditioning to ∼0.02 V during cycle #3, correlating with the initial impedance decrease. Starting at cycle #28, the cell voltage starts to increase from 0.01 V to a maximum of 0.11 V in cycle #68. This overpotential increase is even better visible for the "1*C*" cycles (≡ 3.0 mA or 1.50 mA/cm^2_{Li}): here, the overpotential increases from 0.16 V (#7) to 0.20 V (#27), to 0.38 V (#47), all the way to 1.34 V (#67).

When calculating the effective lithium/lithium cell resistance from the potential drop of 0.073 V (from -0.119 V to −0.046 V) after 1 s at the end of "discharge" for cycle #68 at a current of 0.30 mA (as it is done for direct current internal resistance (DCIR) measurements), a value of 243 Ω is obtained. This equates to an areal cell resistance of 486 Ω·cm^2_{Li} (based on the area of the lithium electrodes of 2.0 cm^2_{Li}) or, if referenced to the resistance of only one of the two lithium electrodes, to 243 Ω·cm^2_{Li}. As the lowest frequency of 100 mHz in the EIS measurements shown in Fig. 2 corresponds to a time constant of $T = 1/\omega = 1/2\pi f \approx 1.6$s, the above determined effective cell resistance is in good agreement with the measured low-frequency resistance (LFR, measured at 100 mHz) of 240 Ω·cm^2_{Li} for cycle #68 (see brown spectrum in Fig. 2).

We assign the initial decrease of the magnitude of the real and imaginary impedance to the increase of the surface area upon plating and stripping of lithium metal, i.e., to the commonly observed formation of a porous or mossy lithium surface.[48,50,51] In addition, however, the repeated deposition and stripping of lithium upon cycling continuously produces a fresh lithium metal surface, concomitant with a continuous reduction of electrolyte components for the formation of the SEI. Therefore, we believe that the drastic increase of the HFR is caused by the decomposition of the alkyl carbonate electrolyte solvents, resulting in large amounts of porous SEI and eventually leading to electrolyte dry-out.[52,53]

Nevertheless, the magnitude of the imaginary impedance value at a frequency of 180 mHz (marked by the empty circles in Fig. 2) never exceeds the value of 7.2 Ω·cm^2_{Li} (marked by the horizontal dashed dark blue line) that is observed for cycle #0 during the entire cycling procedure up to cycle #68. Therefore, the contribution of a lithium metal counter electrode to the imaginary impedance at 180 mHz of an NCM/Li cell is <4 % for the here observed imaginary impedance of the NCM working electrode of >200 Ω·cm^2_{WE}. In turn, this means that the NCM capacitance determined from the cell impedance by using -Im($\mathbf{Z}_{cell}$) at 180 mHz in Eq. 1 (i.e., not requiring a reference electrode) would differ by <4 % from the more accurate NCM capacitance value determined from -Im($\mathbf{Z}_{NCM}$) at 180 mHz that can only be obtained for a cell setup with a µ-RE. Thus, a reasonably accurate quantification of a CAM working electrode can be obtained from the cell impedance of a CAM/Li half-cell, if the negative imaginary impedance at 180 mHz is on the order of >200 Ω·cm^2_{WE} (assuming similarly sized working and counter electrode sizes).

Validation of battery cycler impedance by commercial capacitors.—Due to the higher price and the limited availability of potentiostats built for impedance spectroscopy as compared to conventional battery cyclers that usually have no built-in impedance capability, it would be convenient to be able to measure the impedance at the frequency point of 180 mHz using a simple battery cycler, as this would allow for a reasonably accurate quantification of the CAM capacitance from CAM/Li half-cells during the screening of new CAMs. For this purpose, an alternating current was simulated at the Maccor battery cycler by applying a sine-like current-step function with which the current is changed every 100 ms. To validate this approach, the impedance of two types of commercially available capacitors was obtained with the Maccor battery cycler and compared to the precise value determined with the Biologic potentiostat, both depicted in Fig. 3.

Figure 3a shows the measurement data obtained by the Maccor battery cycler (empty circles) and the mathematical fit (line) of the current-step based perturbation (blue) with an amplitude of 0.02 mA and a frequency of 180 mHz applied to one of the electrolytic capacitors. The respective voltage response (red) is delayed as compared to the current and shows an amplitude of ∼19 mV oscillating around an OCV of −40 mV. To calculate the complex impedance of the received signal, data processing was done by fitting the modulated current and the voltage response to a sine curve. This was done by first subtracting a baseline from the signal to account for voltage drifts by calculating a floating average of the voltage with the bandwidth of one sine period (target value: 180 mHz, effectively 5.6 s at 178.56 mHz). After subtraction, the current and the voltage were fitted to Eqs. 2 and 3, respectively, using an applied frequency of $\omega_0 = 2\pi f_0 = 2\pi \cdot 178.58$Hz, yielding the fitting parameters for the current amplitude (I_0), the voltage amplitude (U_0), as well as the phase of current (φ_I) and voltage (φ_U). The relative phase shift was calculated by $\varphi_0 = \varphi_U - \varphi_I$.

$$I(t) = I_0 \cdot \sin(\omega_0 t + \varphi_I) \quad [2]$$

$$U(t) = U_0 \cdot \sin(\omega_0 t + \varphi_U) \quad [3]$$

From the fit in Fig. 3a, the relative phase shift φ_0 of the two curves was identified to correspond to −1.39 s for the electrolytic capacitor, equating to approximately $-\pi/2$ or −90° (precisely −89.4°), considering the duration of a period of 5.56 s. From the fitting parameters I_0, U_0, and φ_0, the real and the imaginary impedance were calculated by the following formula:

$$\mathbf{Z} = \frac{|U_0|}{|I_0|} \cdot e^{i\varphi_0} = \frac{|U_0|}{|I_0|} \cdot \cos(\varphi_0) + i \cdot \frac{|U_0|}{|I_0|} \cdot \sin(\varphi_0) = \mathrm{Re}(\mathbf{Z}) + i \cdot \mathrm{Im}(\mathbf{Z}) \quad [4]$$

The calculated impedance values at 180 mHz obtained for the electrolytic capacitors by the Maccor battery cycler are depicted in Fig. 3b (empty triangles), together with the impedance spectra collected using the Biologic potentiostat (line), including the respective value at 180 mHz (empty circles). The impedance of the electrolytic capacitors consists of a vertical line through the origin (corresponding to a phase shift of $\varphi_0 = -90°$, as it would be expected for an ideal parallel-plate

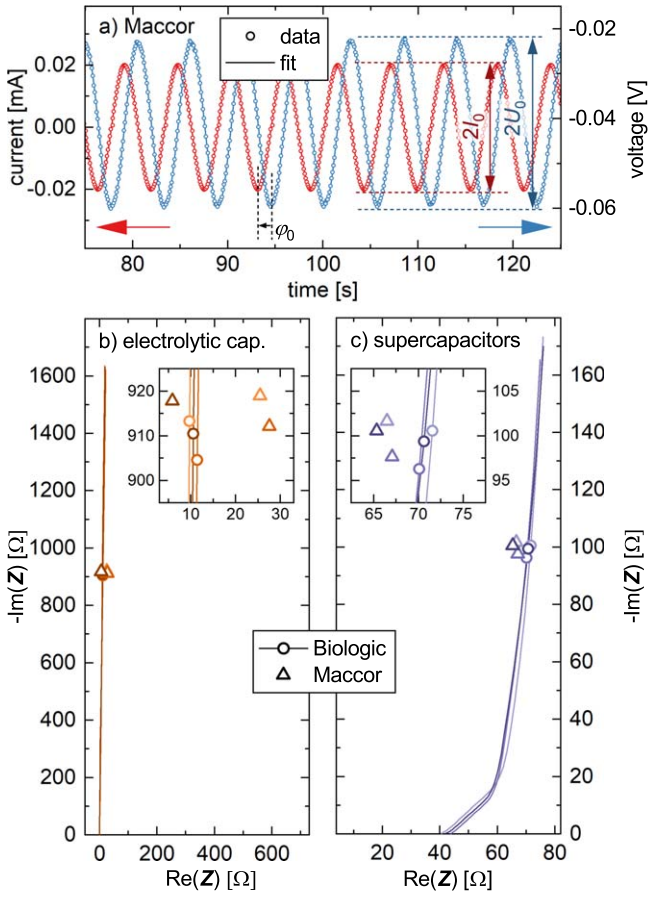

Figure 3. Impedance data of three replicas each of a 1 mF electrolytic capacitor as well as of a 10 mF supercapacitor at OCV and 25 °C, determined by PEIS with an amplitude of 15 mV from 100 kHz to 100 mHz using the Biologic potentiostat as well as by a single-point GEIS at 180 mHz with an amplitude of 0.02 mA for the electrolytic capacitor and 0.2 mA for the supercapacitor using the Maccor battery cycler. **a)** Measurement data (empty circles) and mathematical fit (line) of the current-step-based perturbation (blue) and the voltage response (red) of an electrolytic capacitor measured at 180 mHz with the Maccor battery cycler. The relative phase shift as well as the twofold amplitudes of current (I_0) and voltage (U_0) are marked by the dashed lines and the arrows. Nyquist plots of **b)** the electrolytic capacitors (three shades of ocher) and of **c)** the supercapacitors (three shades of violet), showing the PEIS data (Biologic, lines) including the frequency point at 180 mHz (empty circle) as well as the GEIS data at 180 mHz (Maccor battery cycler, empty triangles).

capacitor). The impedance obtained at the Biologic potentiostat at 180 mHz shows a real value of Re(**Z**) = 10.5 ± 0.9 Ω and an imaginary value of -Im(**Z**) = 909 ± 4 Ω, which we believe to be more precise owed to an instrument architecture that is optimized for impedance measurements. At the Maccor battery cycler, the impedance shows a real value of Re(**Z**) = 16.8 ± 10.9 Ω and an imaginary value of -Im(**Z**) = 915 ± 3 Ω. The larger scatter of the real value is attributed to small errors in the obtained phase shift: As the value of the real impedance is relatively small at a phase angle of around ±90° whereas the imaginary value is relatively large, small deviations of the phase angle lead to a large relative error of the real impedance value, as it is proportional to cos(φ_0). In contrast, the obtained imaginary value (proportional to sin(φ_0)) is not affected significantly by small errors in the phase angle, as already discussed in part I of this study.[34]

In turn, however, if a relatively large shift of the capacitive branch in the real direction would occur (possibly due to, e.g., a large contact resistance of uncompressed electrodes, ohmic resistances of the setup, etc.), the phase angle of the impedance vector φ_0 for the 180 mHz point would become smaller (i.e., $0 < \varphi_0 \ll \pi/2$). Hence, a certain error in the determination of the phase angle at the Maccor could lead to significant deviations of the extracted imaginary impedance value and, therefore, of the capacitance. Even though this seems unlikely in practical cases, as the real part of an electrode/cell should be low for a proper application, the extent of this compromise is dependent on the parameters of the systems and on the precision of the measurement. To exclude any erroneous interpretation of the collected impedance data, it is recommended to evaluate both imaginary and real value of the impedance at 180 mHz to be able to estimate any introduced errors.

By using Eq. 1, the capacitance of the electrolytic capacitors is obtained from the frequency points at 180 mHz, yielding similar values of 0.972 ± 0.003 mF (standard deviation based on three capacitor replicas) using the Maccor battery cycler and of 0.980 ± 0.004 mF using the Biologic potentiostat. The deviation between the measured values and the nominal value of 1 mF is well within the tolerance of the specified capacity of the electrolytic capacitor (±20 %).

The impedance spectra of the three replicas of the supercapacitors (depicted in Fig. 3c) include a high-frequency resistance (owed to the ohmic resistance of the electrolyte), a 45° line at medium frequencies (attributed to the ionic electrolyte resistance within the pores of the carbon electrodes),[45] as well as a capacitive branch at low frequencies in the form of a constant-phase element with a phase angle of $\alpha \approx 0.95$.[54] It thus exhibits similar features as one would observe with porous battery electrodes.[46,55] The obtained imaginary values at a frequency of 180 mHz are -Im(**Z**) = 100 ± 2 Ω using the Biologic potentiostat and -Im(**Z**) = 98 ± 2 Ω using the Maccor battery cycler; based on Eq. 1, the resulting values for the capacitance of the supercapacitors are 9.0 ± 0.2 mF using the Biologic potentiostat and 8.9 ± 0.2 mF using the Maccor battery cycler. The deviation between these measured capacitances and the nominal value of 10 mF is well within the specified product tolerance of −20 %/+80 %.

To summarize the above discussion, it can be stated that the relative error of the capacitance values obtained from the current-step-based simulated sine-form current perturbation at 180 mHz with the Maccor battery cycler as compared to the capacitance values obtained with the Biologic potentiostat is found to be <1.5 % for both types of capacitors. This demonstrates the feasibility and the validity of the here developed method to determine the cell capacitance with a simple battery cycler by simulating a sine-form current perturbation at 180 mHz using a current-step based procedure that can be easily programmed.

Application in a simplified coin half-cell setup.—After investigation of the applicability of a two-electrode setup with a lithium metal anode for the determination of the NCM electrode capacitance as well as the possibility of conducting the measurement with a simple battery cycler, a "real" cell system will be investigated next. Figure 4a shows the initial OCV, the initial EIS in the pristine state, the conditioning, and the first formation cycle of a coin half-cell with an NCM851005 cathode and a lithium metal anode, conducted with the Maccor battery cycler. After the initial OCV phase, the cell was discharged to 2.55 V_{Li}, where a CV step was applied until the current dropped below *C*/250 (~0.0073 mA/cm$^2_{WE}$). Under the assumption that the residual current at this point is approximately constant over the time frame of several tens of seconds, a sine curve with a current amplitude (i_0) corresponding to *C*/50 (0.036 mA/cm$^2_{WE}$) was modulated on top of the residual current (marked by *pristine*, with a variation of the current between 0.044 and −0.029 mA/cm$^2_{WE}$). After the initial PEIS, the cell was charged to ~10 %SOC (marked by A), then (Z_{cell}-Li-M, see Table I) discharged to 2.55 V_{Li} (B), where another CV hold at 2.55 V_{Li} (B) and a PEIS (marked by cycle #0) was performed. The cell was then charged (C) and discharged at *C*/10 (first formation cycle, ending at D) before the capacitance test was repeated after another CV hold at 2.55 V_{Li} (marked by cycle #1). Figure 4b shows the enlarged view of the applied current modulation at 180 mHz (via the current-step procedure) and the voltage response after the first formation cycle (cycle #1). Although the average current

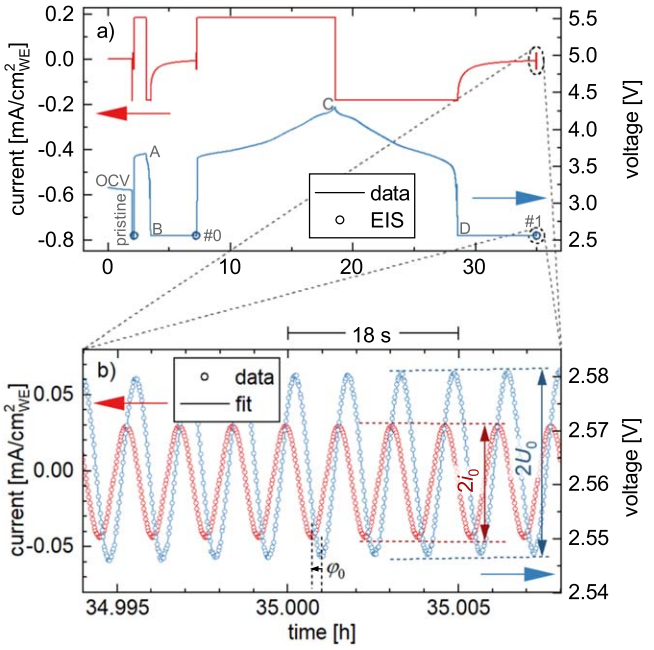

Figure 4. Current and potential profile of the initial cycling in a coin NCM/Li half-cell (Z_{cell}-Li-M, see Table I) measured with the Maccor battery cycler using a current-step simulated sine-form current perturbation with 180 mHz. **a)** Area-normalized current (red, left axis) and voltage (blue, right axis) of the conditioning and first formation cycle. After an OCV period of 2 h, the cell is brought into blocking conditions by discharging to 2.55 V_{Li} in CCCV mode (until the current dropped below *C*/250), after which the capacitance measurement is performed (see main text). In a conditioning step, the cell is then charged to ∼10 %SOC (marked by A), before the cell is again discharged to 2.55 V_{Li} (B), where the capacitance is again determined (marked as cycle #0). The cell is then charged to 4.3 V_{Li} (C) and again discharged (D) for a full formation cycle after which the capacitance is again determined (cycle #1). **b)** Enlarged view of the current perturbation at the end of the first formation cycle. The measured values are shown as empty circles, with the fitted sine curves being shown as solid lines. The area-normalized current amplitude (i_0), the voltage amplitude (U_0), and the phase shift (φ_0) are indicated by arrows.

(i.e., the time-averaged current over the cycles shown in Fig. 4b) is not perfectly zero due to the residual current (of less than *C*/250) (see above), a sine wave voltage response with an amplitude of $U_0 = 17$ mV (between 2.54 V_{Li} and 2.58 V_{Li}, see blue symbols/line) is observed. This value is in good accordance with the voltage amplitude of $U_0 = 15$ mV that was chosen for the PEIS measurements with the Biologic potentiostat, validating the chosen dimension of the current perturbation. The phase shift between current and voltage resulting from the fits of current and voltage to Eqs. 2 and 3, respectively (solid red and blue lines in Fig. 4b) amounts to $\varphi_0 = -62.6°$ (corresponding to a time shift of −0.97 s).

For the 180 mHz impedance measurement performed at the Maccor battery cycler, the current instead of the voltage is controlled, as this turned out to be more feasible for the experiment at this instrument, possibly due to the much faster instrument response rates in galvanostatic operation mode. To get reproducible results for the specific capacitance of the electrodes, the applied current perturbation must be sufficiently small to induce only minor changes (below ±50 mV) on the electrode potential of the previous CV phase, as the double layer capacitance of the electrochemically active materials (CAM, Li, conductive carbon) is potential dependent. Thus, the perturbation current is modulated on top of the base current at the end of the CV phase to stay in the potential range of 2.55 V_{Li}, as otherwise the perturbation would be modulated on top of the OCV relaxation curve. This base current (here: 0.0073 mA/cm$^2_{WE}$) is assumed to stay constant over the measurement range (40 sine periods à 5.6 s, in total 224 s). However, the residual current at the end of the CV step after the first cycle (cycle #1) still changes at a rate of ∼0.001 μA/s·cm$^2_{WE}$ during impedance measurement at 180 mHz shown in Fig. 4b (corresponding to ∼0.2 μA/cm$^2_{WE}$ over the 40 sine waves). This, in combination with limitations in the hardware of the battery cycler (latency when switching between charge and discharge) leads to a slight drift in the voltage during measurement. This shift was <0.01 V for all performed measurements and was accounted for by the baseline subtraction of the floating average.

Additionally, the difference of time spent at 2.55 V_{Li} in the CV step prior to an impedance measurement needs to be discussed, as the impedance measurements were performed either in potentiostatic mode (PEIS) with the Biologic potentiostat or in galvanostatic mode (GEIS) with the Maccor battery cycler: the average time to reach the cutoff criterion of *C*/250 at 2.55 V_{Li} for the GEIS measurements is on the order of 5 h, in comparison to the 1 h CV hold at 2.55 V_{Li} performed before the PEIS measurements, increasing the experimental time for a set of 5 cycles by ∼15 %. In theory, this longer duration might affect the measurement due to phenomena like calendar aging of the NCM and the lithium metal within the cell.[56,57] In comparison to other occurrences like the continuous SEI growth during lithium metal plating and stripping, this impact is assumed to be negligible.

Similar to conventional EIS measurements performed over the whole frequency range, the single-point GEIS measurement using a current-step-based sine wave modulation is determined by a series of experimental parameters: the voltage where blocking conditions are achieved (here: 2.55 V_{Li}), the time/current over which this voltage is held before the low-frequency modulation happens (here: until the current drops below *C*/250), the applied frequency of the alternating current (here: 180 mHz), and its amplitude (here: *C*/50). Those parameters can be varied and adapted to the individual case as long as certain boundary conditions are still met, e.g., the charge-transfer resistance still being semi-infinitely large. The base current on which the alternating current is applied can be further reduced to decrease the overall measurement time if no severe voltage drift during modulation is observed. The frequency was chosen due to the mathematically small deviation of the constant-phase element in comparison to the behavior of an ideal capacitor, but can be varied in a certain range if this factor is regarded.[34] The amplitude can be adapted to the measured voltage response, so that a proper signal-to-noise ratio is achieved, should however not be increased in a way that the SOC is significantly varied over the range of a single sine excitation. In our view, it might be advantageous if material developers would use battery cyclers having an implemented option to include (potentiostatic and/or galvanostatic) single-frequency impedance points (at relatively low frequency of ∼180 mHz) in testing protocols.

Comparison of the different NCM cell configurations.—Finally, a direct comparison of the capacitance data with different cell and test hardware configurations was realized. When transferring the formerly established approach to determine the CAM capacitance using a T-cell setup with a μ-RE and operated with an impedance-capable potentiostat[34] into an approach based on coin half-cells operated with a simple battery cycler, the impact of the following changes made must be evaluated: (i) moving from a cell setup with a μ-RE to a two-electrode setup without μ-RE; (ii) replacing the pre-lithiated LTO counter electrode with a lithium metal counter electrode; and, (iii) conducting the impedance measurement with a common battery cycler without explicit impedance capability (Series 4000, MACCOR) rather than with a PEIS-capable potentiostat (VMP3, Biologic). Table I gives an overview of the cells built for this purpose.

Figure 5a shows the Nyquist plot of all cell combinations at 2.55 V_{Li} after the initial conditioning step (cycle #0). The cathode impedance spectrum measured by the T-cell setup with μ-RE at the Biologic potentiostat (cell Z_{NCM}-LTO-B; as originally described in

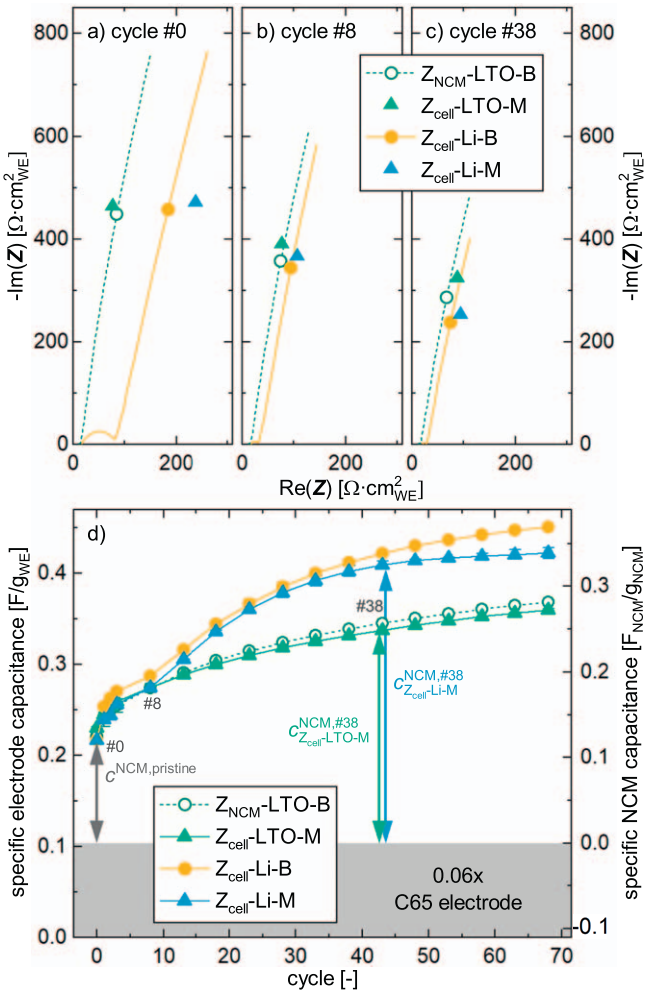

Figure 5. Impedance spectra and specific capacitance vs. cycle number for the four different combinations of cell setups and measurement modes, all based on an NCM working electrode (specified in Table I). Nyquist plots recorded in blocking conditions shown after **a)** initial conditioning (cycle #0), **b)** after cycle # 8, and **c)** after cycle #38. For the cells measured at the Biologic potentiostat, the measurement over the whole frequency range is given by the dashed dark green line (T-cell with μ-RE and LTO anode: Z_{NCM}-LTO-B) and by the yellow solid line (coin cell with a lithium metal anode: Z_{cell}-Li-B), with the 180-mHz frequency points highlighted as circles. For the measurements done at the Maccor battery cycler using a current-step-based sine wave modulation at 180 mHz, the impedance at 180 mHz is given as green triangle for the coin cell with the LTO anode (Z_{cell}-LTO-M) and as blue triangle for the coin cell with the lithium metal anode (Z_{cell}-Li-M). **d)** Specific electrode capacitance in units of F/g_{WE} (left *y*-axis) and the specific NCM capacitance in units of F_{NCM}/g_{NCM} (right y-axis), both as a function of the cycle number, shown for the NCM working electrode for the T-cell with μ-RE or for the entire cell for the coin cells. The gray box indicates the contribution of the binder-carbon mixture of 0.104 F/$g_{electrode}$ to the total capacitance. The specific capacitance of the NCM (right y-axis) was obtained by subtracting the contribution of C65 and PVDF from the value of the entire electrode, schematical shown by the arrows in cycle #0 and #38, and subsequently normalizing it to the NCM mass contribution (of 94 wt%) in the electrode. The values of the capacitance shown here are calculated from the mean of two identical cell pairs and the error bars correspond to the minimum/maximum value of two measurements.

part I and part II of this study[34,36]) is shown in dark green, mainly consisting of a capacitive branch, whereby the empty circle highlights the 180-mHz frequency point. For the NCM851005 working electrode, a real impedance of Re($\mathbf{Z}_{NCM}$) = 84.9 Ω·cm²$_{WE}$ and an imaginary impedance of -Im($\mathbf{Z}_{NCM}$) = 447.5 Ω·cm²$_{WE}$ is obtained ($\varphi_0 = -79°$) at 180 mHz. This can now be compared to the pseudo full-cell impedance measured at 180 mHz at the Maccor potentiostat in a two-electrode coin cell setup, still employing a pre-lithiated LTO anode (green triangle, cell Z_{cell}-LTO-M). By fitting the voltage response to the current perturbation with a frequency of 180 mHz, a real impedance of Re($\mathbf{Z}_{cell}$) = 77.3 Ω·cm²$_{WE}$ and an imaginary impedance of -Im($\mathbf{Z}_{cell}$) = 462.8 Ω·cm²$_{WE}$ is obtained ($\varphi_0 = -81°$), being reasonably close to the one of the μ-RE setup, as expected from the observations made in Fig. 1. When comparing these data with the cell impedance of the coin half-cell, where lithium metal is employed as counter electrode (cell Z_{cell}-Li-B, measured with the Biologic potentiostat, yellow line), a shift of the capacitive branch at low frequencies to higher real impedance values is observed, caused by an additional semicircle feature at high frequencies. This is consistent the measured impedance of the pristine symmetrical lithium/lithium cell shown in Fig. 2: As the impedance of the complete cell is measured, the impedance response is a superposition of the lithium metal and the NCM impedance; therefore, a higher value is determined for the real part, namely Re($\mathbf{Z}_{cell}$) = 184.0 Ω·cm²$_{WE}$. However, due to the small contribution of the real impedance to the imaginary impedance at the 180-mHz point (see yellow circle in Fig. 2), the effect of replacing the LTO counter electrode with a lithium counter electrode on the imaginary part of the impedance is only minor, resulting in a value of -Im($\mathbf{Z}_{cell}$) = 456.3 Ω·cm²$_{WE}$ which is very close to the value that was obtained with the T-cell with a μ-RE (Z_{NCM}-LTO-B) that yielded a value of -Im($\mathbf{Z}_{NCM}$) = 447.5 Ω·cm²$_{WE}$. Finally, the blue triangle depicts the 180-mHz point for the same coin half-cell setup measured with the Maccor battery cycler (cell Z_{cell}-Li-M). Even though the real part is shifted to higher values with Re($\mathbf{Z}_{cell}$) = 237.8 Ω·cm²$_{WE}$, the imaginary part of -Im($\mathbf{Z}_{cell}$) = 469.9 Ω·cm²$_{WE}$ again fits well with the values obtained from the other configurations. The observed shift in the real part is hereby assumed to originate from the lithium metal anode impedance, which is expected to stem from cell-to-cell variations occuring for the initially low surface area of the employed lithium foil, where small differences in the NCM loading determines the amount of exchanged charge (and thus freshly plated lithium surface), and can therefore have a significant impact on the measured impedance. Likewise, deviations in the areal resistance can also originate from varying areal loadings of the NCM active material itself, which, however, will be eliminated for Fig. 5d when normalizing the capacitance to the electrode mass.

Furthermore, it must be considered that a single-point impedance is not sufficient to determine whether the CAM is in blocking conditions, i.e., whether the 180-mHz point lies on the capacitive branch in the Nyquist depiction or whether it lies on another semicircular feature in the case that the semi-infinite charge-transfer resistance might not be reached. For NCMs, no deviation of the capacitive behavior was observed so far; however, it is recommended to measure an impedance spectrum over the whole frequency range to understand the impedance behavior of the CAM that is being investigated before going forward with single-point measurements using a battery cycler.

Figures 5b and 5c show the Nyquist plots after cycle #8 and #38, respectively. For all cells, a continuous decrease of the negative imaginary contribution of the 180-mHz point is observed, coinciding with the cycling-induced increase of the capacitance of the CAM by particle fracture and, therefore, of the surface area. Similar to the lithium/lithium cell impedance shown in Fig. 2, a decrease of the real part of the cell impedance at lower frequencies as well as of the semicircle is observed for the half-cell setups. Although the values measured with the Biologic potentiostat and the Maccor battery cycler coincide well in all cases, the decrease of the negative imaginary contribution to the impedance at 180 mHz undergoes a stronger decrease for the cells measured vs. a lithium metal counter electrode: from cycle #0 to #38, the imaginary part decreases from -Im($\mathbf{Z}_{NCM}$) = 447.5 Ω·cm²$_{WE}$ to -Im($\mathbf{Z}_{NCM}$) = 285.6 Ω·cm²$_{WE}$ for the Z_{NCM}-LTO-B cells as well as from -Im($\mathbf{Z}_{cell}$) = 456.3 Ω·cm²$_{WE}$ to -Im($\mathbf{Z}_{cell}$) = 237.4 Ω·cm²$_{WE}$ for the Z_{cell}-Li-B cells. This will be further discussed in the following.

Figure 5d shows the evolution of the specific capacitance of the NCM electrode (left y-axis) as well as of the NCM active material only (right y-axis), as determined from the imaginary impedance as a function of cycle number for all four examined cell and test hardware configurations. The values for the specific electrode capacitance were calculated by Eq. 1 using the imaginary cell impedance or NCM impedance (in case of cell Z_{NCM}-LTO-B) at 180 mHz. After conditioning (cycle #0), all measurements are in good agreement. Exemplarily for the Z_{NCM}-LTO-B cell, a specific capacitance of 0.221 ± 0.008 F/g_{WE} is obtained which then increases to a value of 0.255 ± 0.007 F/g_{WE} over the three formation cycles (green empty circles in Fig. 5d, left y-axis). To determine the capacitance of the NCM active material only, from which the relative surface area increase of the NCM CAM can be deduced, the contribution of conductive carbon and binder to the capacitance must be subtracted. The latter was estimated by the measurement of a model electrode without NCM, as outlined in part I of this study; for the present study, the contribution by the conductive carbon and the binder is 0.104 ± 0.002 F/g, corresponding to 6 % of the capacitance of the C65/PVDF electrode (with a composition of C65:PVDF of 1:1 w/w) of 1.729 ± 0.028 F/g, since the NCM electrode comprises 6 wt% of the C65/PVDF mixture.[34] After this subtraction of the contribution of the conductive carbon and the normalization by the mass of the active material, a value for the NCM specific capacitance of 0.125 ± 0.005 F_{NCM}/g_{NCM} is determined (plotted vs. the right y-axis in Fig. 5d). By using the value for the surface-area-normalized capacitance for NCMs of ∼28 $\mu F_{NCM}/cm^2_{NCM}$ in LP57 at 2.55 V_{Li} determined in part II of this study,[36] the obtained value for the specific NCM capacitance can be converted to a specific surface area of ∼0.4 m^2_{BET}/g_{NCM}, which is approximately twice as large as compared to the value of the pristine NCM powder determined by N_2-BET. This difference is attributed to the cracking and the concomitant surface area increase of the secondary NCM agglomerates due to the mechanical forces during calendering, as reported previously.[34,35,58] It should be noted that, for carbons, the surface-area-normalized capacitance (e.g., of VGCF or C65) with typical values between 4 and 10 $\mu F/cm^2$ is significantly smaller.[34,59]

During the first three cycles, an increase of the capacitance value to 0.161 ± 0.003 F_{NCM}/g_{NCM} is observed for all four cell setups what equals an increase of ∼30 % as compared to the initial NCM capacitance. Depending on the upper cutoff potential, the capacitance increase of an NCM622 CAM evaluated in the first part of this study varied from ∼50 % (3.9 V) to ∼100 % (4.5 V),[34] which is much higher as compared to the NCM851005 used in this study. When comparing different CAMs, a higher tendency for particle fracture would be expected for compositions that have a higher nickel content, as the degree of delithiation that is reached up to a set voltage, and thus the anisotropic volume contraction, increases.[32,40,60] However, in part I of this study,[34] uncalendered electrodes were used for the determination of the capacitance evolution upon cycling; here, however, the NCM851005 electrodes were calendered before use, which is always done for electrodes used in commercial cells to maximize the energy density. Due to this compression, the mechanical cracking of the polycrystalline particles increases the electrode surface area already before cell assembly, as this was shown in part I of this study,[34] what is partially responsible for the smaller relative surface area increase upon cycling of the here examined NCM851005 cathodes compared to the NCM622 cathodes that had been uncalendered. Additionally, the size and the shape of the NCM primary crystallite as well as the morphology of the secondary NCM particle agglomerates have an impact on the relative surface area increase upon cycling.

Next to the differences in mechanical processing of the electrode tapes or the CAM type, other factors might affect the capacitance that is determined initially for the pristine cell: Commercial CAMs are frequently washed to remove residual lithium salts such as Li_2CO_3 and LiOH,[61,62] which remain from the synthesis procedure or form during improper storage of the materials.[63–66] Said washing, e.g., impacts the surface area accessible for the electrolyte by opening initially clogged pores within the secondary particle agglomerates. Even though the pristine capacitance varies for differently prepared CAMs and electrodes thereof, a quantitative comparison of the capacitance upon cycling is still reasonable: as the areal capacitance of NCM materials was identified to be 25 $\mu F/cm^2_{CAM}$ independent of nickel content or particle morphology, as shown in part II of this study,[36] the determination of the NCM capacitance directly provides the surface area of the active material in the cell, which is in many cases directly proportional to the various side reactions of the positive electrode, such as oxygen release, electrolyte decomposition, formation of a resistive oxygen-depleted surface layer, and transition metal dissolution, as discussed in the introduction. Therefore, this method provides a powerful tool for the large-scale investigation and optimization of CAMs in material development.

When considering the capacitance evolution over the measured range of 68 cycles, no significant difference between the two test hardware configurations (Biologic vs. Maccor) as well as between the electrode setups (with and without μ-RE) is observed for the cells with an LTO counter electrode, with the estimated NCM capacitance being 0.282 ± 0.005 F_{NCM}/g_{NCM} (cells Z_{NCM}-LTO-B in Fig. 5d, right y-axis) and 0.273 ± 0.005 F_{NCM}/g_{NCM} (cells Z_{cell}-LTO-M), i.e., differing by <4 %. However, a divergence of the cells with a lithium metal counter electrode in comparison to those with an LTO counter electrode develops after cycle #8: while the NCM capacitance values of the NCM/Li cells up to cycle #38 agree reasonably well with each other (0.328 ± 0.006 F_{NCM}/g_{NCM} for Z_{cell}-Li-B vs. 0.318 ± 0.007 F_{NCM}/g_{NCM} for Z_{cell}-Li-M after 38 cycles), they are substantially higher than those obtained for the NCM/LTO cells (0.250 ± 0.001 F_{NCM}/g_{NCM} for Z_{NCM}-LTO-B vs. 0.242 ± 0.001 F_{NCM}/g_{NCM} for Z_{cell}-LTO-M after 38 cycles). Upon further cycling of the NCM/Li cells, the NCM capacitance values obtained with the Maccor battery cycler are slightly lower compared to those obtained with the Biologic potentiostat (e.g., in cycle #68, 0.339 ± 0.007 F_{NCM}/g_{NCM} for Z_{cell}-Li-M vs. 0.370 ± 0.006 F_{NCM}/g_{NCM} for Z_{cell}-Li-B). At the cycle number where the divergence of the data measured with the two different test hardware configurations (Maccor battery cycler vs. Biologic potentiostat) initiates, the impedance of the lithium metal anode already starts to significantly rise, as depicted in Figs. 2 and A·1. Although it is not clear if the deviation between the two test hardware configurations is correlated to this impedance rise, the limitations of the CAM/Li half-cells upon extended cycling become obvious, indicating that the capacitance measurement in half-cells should be restricted up to a certain number of cycles, or exchanged accumulated charge per area of the lithium metal anode, respectively.

For the above discussed reasons (i.e., the minor contribution of the lithium metal anode to the imaginary part of the impedance), the larger increase of specific NCM capacitance of the NCM/Li cells starting at cycle #8 cannot be ascribed to a cell-to-cell variation nor to a measurement artifact but originates from a real increase of the CAM's surface area. Even if the lithium metal anode would develop a significant contribution to the imaginary impedance, an increasing imaginary impedance would indicate a drop in capacitance following Eq. 1 instead of the measured increase. As the lithium metal electrode can barely decrease to lower values, as no imaginary impedance of $-\mathrm{Im}(\boldsymbol{Z}) < 0$ is expected (see Fig. 2), the additional increase in the capacitance is, therefore, assigned to a true decrease of the imaginary impedance of the cathode. Here, cross-talk phenomena between the lithium metal anode and the CAM that do not come into play for the LTO anodes must be considered,[67] whereby an apparent difference between an LTO and a Li counter electrode is that no SEI is formed on an LTO electrode due to its significantly higher electrode potential of 1.55 V_{Li} and that it does not form any additional surface area as no lithium plating can occur. Indeed, it is expected that impurities like alkoxides, soluble electrolyte reduction products, and/or detached SEI components, all originating from the lithium metal surface of the counter

electrode, can be oxidized at the cathode potential, leading to the formation of protons within the electrolyte.[68] Said protons can hydrolyze residual Li_2CO_3 impurities in CAMs that stem from synthesis or storage.[69] If said Li_2CO_3 residuals sit at the grain boundaries between the primary particle crystallites of the secondary NCM agglomerates, the dissolution process is hypothesized to lead to a capacitance increase as a result of pore opening and a concomitant increase of the electrolyte percolation within the secondary agglomerates.

Although it can only be hypothesized on the contribution of the electrolyte to the increased surface area, a clear difference in the coulombic efficiency can be seen when comparing cells with LTO vs. those with a lithium metal counter electrode, as shown in Fig. A·2b. The oxidation of the impurities formed at the counter electrode and oxidized on the cathode electrode would be expected to provide additional electrons on the cathode side, what would result in a higher charge or lower discharge capacity for each cycle. While the coulombic efficiency of the NCM/LTO cells averages >0.995 over the whole cycle range, a lower coulombic efficiency of ~ 0.98 is measured for the NCM/Li cells, indicating parasitic side reactions on the NCM cathode. In fact, the coulombic efficiency continuously decreases during the cycling of the NCM/Li cells, which coincides with the increase of lithium metal surface area by plating and stripping operation, facilitating said parasitic reactions, which thus could explain said continuous decrease of the coulombic efficiency by increasing the extent of a parasitic current. In addition, when investigating the discharge capacities depicted in Fig. A·2a, a slightly steeper capacity fading is observed for the cells with a lithium metal counter electrode as compared to the ones with an LTO counter electrode, starting at around cycle #20 and indicating a faster NCM degradation for the NCM/Li cells, possibly originating from the above described cross-talk phenomenon.

Overall, these observations indicate a distortion of the capacitance and the coulombic efficiency when NCM electrodes are tested for many cycles in a half-cell setup. To reduce the effect of the cross-talk to a minimum, we therefore suggest limiting the amount of half-cell cycles to <10. This approach was already applied successfully to evaluate the effect of the morphology on the electrochemical behavior of $LiNiO_2$.[70] When seeking to evaluate the morphological stability that would be exhibited by a given active material over extended charge/discharge cycling in a full-cell, it is recommended to avoid the use of lithium metal counter electrodes, as this would lead to cross-talk-induced artefacts (see above). For this purpose, the counter electrode should instead be based on other active materials that also satisfy the prerequisites of a relatively low imaginary contribution at low frequencies (of $\sim$180 mHz) and a sufficient lithium reservoir to fully lithiate the working electrode upon discharge to induce blocking conditions (e.g., graphite, LTO, or LFP, all capacitively oversized and used in a partially lithiated state).

In principle, the developed approach should also be applicable for other active materials including anode active materials, if they can be brought into blocking conditions. Of course, the same prerequisites apply, i.e., a counter electrode with a relatively low imaginary impedance contribution at low frequencies (of $\sim$180 mHz) is required. Throughout this study, in addition to the different NCM compositions and morphologies, the capacitance of conductive carbons (i.e., VGCF and C65) was determined;[34] furthermore, the particle cracking of LFP was quantified by the here presented impedance-based method by monitoring its increasing capacitance upon charge/discharge cycling, while, in contrast, the capacitance of LTO was observed to remain constant in a similar experiment.[34] For graphite active materials, the application of this method does not seem interesting, as no surface area increase due to particle cracking is expected. For silicon, being a possible alternative for graphite on the negative electrode, the evaluation of the capacitance could provide a quantification of the surface area increase induced by the large volume change upon lithiation; however, this approach does not appear to be straightforward since the SEI formation of silicon would likely alter the surface-area-normalized capacitance as well as decrease the electronic conductivity of the silicon electrode.[71,72] In general, monitoring the change of the electrochemical capacitance of anode active materials is expected to be possible using a suitable electrode composition (e.g., using conductive carbons such as VGCF ensuring the sufficient electronic connection of the active material); however, for the operation of electrodes at potentials below the reduction potential of the electrolyte components, the concomitant (possibly continuous) SEI formation must be considered for the meaningful application of this method.

In general, if the parameters of any type of working electrode were to deviate strongly from the typically used values that had been chosen for this study (such as the mass loading of the electrode, its porosity, its contact resistance, the electronic conductivity through the electrode, its initial specific surface area, the ratio of the capacitance contribution of the active material and the other components, etc.), however, the approach using the single-point frequency at 180 mHz in a half-cell for the determination of the capacitance would have to be reevaluated. Exemplarily, in the case of an increased mass loading of the working electrode (or, similarly, an increased specific surface area of the active material powder), the imaginary impedance would decrease due to the increased total surface area, which would consequently increase the relative contribution of the counter electrode to the imaginary impedance, inducing a larger relative error of the capacitance determined for the working electrode. In general, the potential user of the here presented method is advised to thoroughly analyze and fully understand the impedance response of the investigated active materials and electrodes before this simplified method is applied.

Conclusions

In this study, we deduced a stepwise simplification of the experimental design to monitor particle cracking through the evolution of the capacitance of a NCM851005 CAM from the sophisticated, but intricate setup in T-cells with a micro-reference electrode to a conventional coin (half-)cell setup. For the latter, no μ-RE electrode is required if the impedance of the counter electrode is negligible as compared to the investigated CAM working electrode. This prerequisite is met for electrodes such as (pre-lithiated) LTO and likely even for pre-lithiated graphite. Even though lithium metal showed a relatively large impedance, it is still suitable for the use as counter electrode, as its contribution to the imaginary cell impedance at 180 mHz is small as compared to the one of the examined NCM working electrode.

Additionally, it was shown that the NCM capacitance does not have to be extracted from a full impedance spectrum provided by an impedance analyzer but can be obtained by solely a low-frequency single-point impedance measurement performed with a simple battery cycler without explicit impedance capabilities, whereby a sine-like current perturbation at 180 mHz is generated by a stepwise but rapid change of the applied current. The measurement of two types of commercial capacitors resulted in a deviation of <1 % between the two methods.

Each step of the transformation was validated in cycling experiments using four different cell and test hardware configurations: No deviation in the specific NCM capacitance was found for cells without a reference electrode as well as for the single-point impedance measurement at the battery cycler for at least 68 cycles. However, it could be shown that cross-talk phenomena increase the capacitance and, consequently, the electrochemically active surface area of the NCM CAM when cycled against a lithium metal counter electrode for extended cycling. These occurring side reactions with NCM/lithium cells were also expressed in the decrease of the coulombic efficiency in contrast to NCM/LTO cells (i.e., pseudo full-cells).

Even though we suggest limiting the analysis of the capacitance in half-cells to $\sim$10 charge/discharge cycles due to pronounced cross-talk phenomena as compared to NCM/LTO cells, the data

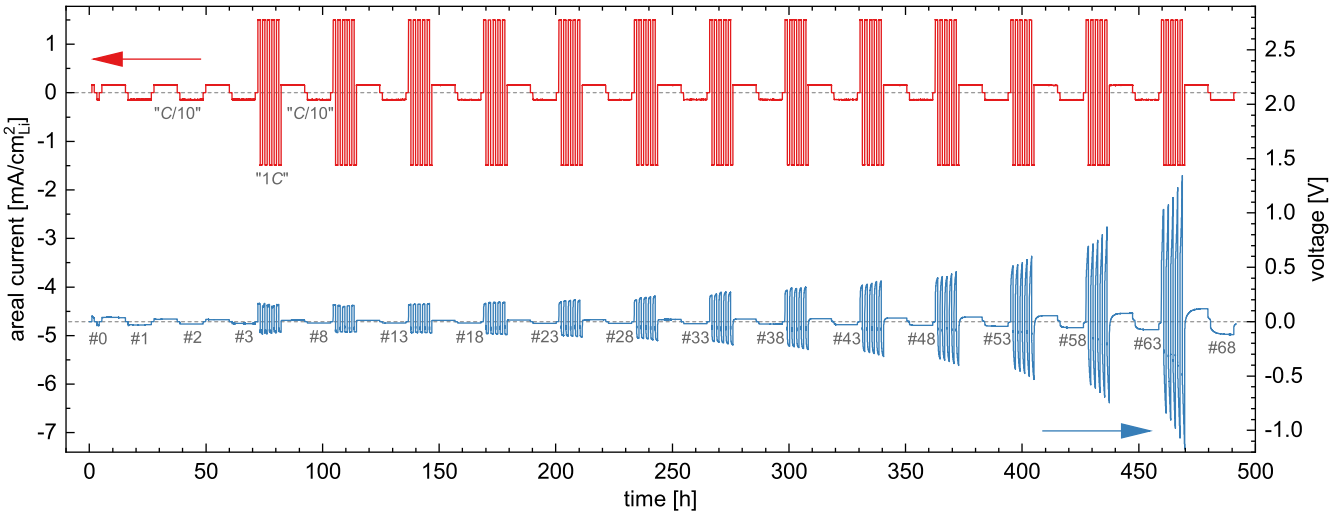

Figure A·1. Cycling data of the symmetric lithium/lithium cell presented in Fig. 2, showing its areal current (red, left axis) and cell voltage profile (blue, right axis). For the "*C*/10" cycles, 0.30 mA or 0.15 mA/cm$^2_{Li}$ (when normalized to the geometric surface area of the lithium metal electrodes) were applied during symmetric cell cycling, whereas for the "1*C*" cycles, a current of 3.0 mA or 1.50 mA/cm$^2_{Li}$ was set. The "*C*/10" cycles are labeled with the respective cycle number. The cell voltages given in the figure represent the cell potential at the end of the last of the four cycles at 3.0 mA.

acquired by the here proposed method and setup can give valuable information about the chemomechanical stability of CAM particles. Therefore, the capacitance method, which is now applicable in combination with the developed simplified cell and test hardware setup, provides a powerful in situ tool to monitor the surface evolution of CAMs, using only standard testing procedures and instrumentation.

CRediT Authorship Contribution Statement

Stefan Oswald: Methodology, Investigation, Writing—Original Draft. Felix Riewald: Methodology, Investigation, Writing—Original Draft. Hubert A. Gasteiger: Conceptualization, Supervision, Writing—Review & Editing.

Acknowledgments

Financial support by the BASF SE through its Research Network on Electrochemistry and Batteries is gratefully acknowledged.

Appendix

Cycling data of the symmetric lithium/lithium coin cell.— Figure A·1 shows the areal current and potential profiles of the symmetric lithium metal cell discussed in Fig. 2. Even though the same two currents (i.e., 0.30 mA and 3.0 mA) were applied repeatedly over 68 cycles, the cell voltage initially decreases during the first few cycles and later increases again. At cycle #28, the cell voltage starts to increase drastically, which is in good agreement with the LFR extracted from the impedance data being recorded after each slow cycle and presented in Fig. 2.

Cycling data of the different NCM cell configurations.— Figure A·2 shows the coulombic efficiencies and specific discharge capacities of the four different cell configurations during the aging cycles at 1*C* that were used in this study. For all samples, the discharge capacity shown in Fig. A·2a starts at 185.5 ± 1.9 mAh/g$_{NCM}$ in cycle #4 and decreases to 172.8 ± 3.0 mAh/g$_{NCM}$ in cycle #68. Although the capacity retention is similar for all samples, the coulombic efficiency depicted in Fig. A·2b differs depending on the selected counter electrode: it stays on a stable level for the cells with pre-lithiated LTO anodes, viz. at >0.995 (pseudo full-cells, dark green empty circles and green triangles), but continuously decreases for the cells with lithium metal as anode, viz., from 0.995 to 0.97 (yellow circles and blue triangles), indicating parasitic side reactions during cell cycling.

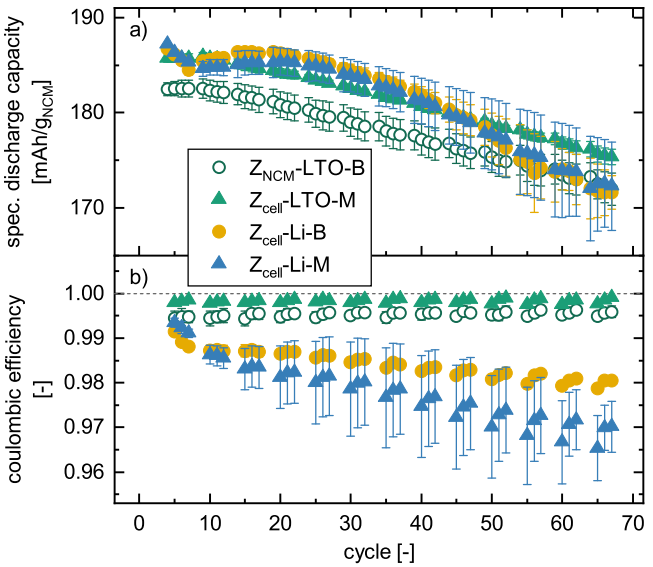

Figure A·2. a) Specific discharge capacity and **b)** coulombic efficiency as a function of the cycle number during the 1*C* cycles for the data depicted in Fig. 5. Green empty circles depict the T-cell setup with a μ-RE and a pre-lithiated LTO anode measured with the Biologic potentiostat (Z$_{NCM}$-LTO-B), green triangles show the coin-cell setup with pre-lithiated LTO anodes measured with the Maccor battery cycler (Z$_{cell}$-LTO-M), yellow circles represent coin half-cells with lithium metal anode measured with the Biologic potentiostat (Z$_{cell}$-Li-B), and blue triangles show the half-cell setup measured with the Maccor battery cycler (Z$_{cell}$-Li-M). The first cycle of each set of four 1*C* cycles was omitted in the presentation of the coulombic efficiency, as the ratio of charge and discharge capacity is affected simply by the change of *C*-rate from *C*/10 to 1*C*. The values shown here are calculated from the mean of two identical cells, and the error bars correspond to the minimum/maximum value of two measurements.

ORCID

Stefan Oswald https://orcid.org/0000-0001-6402-7833
Felix Riewald https://orcid.org/0000-0001-9002-3633
Hubert A. Gasteiger https://orcid.org/0000-0001-8199-8703

References

1. O. Gröger, H. A. Gasteiger, and J.-P. Suchsland, *J. Electrochem. Soc.*, **162**, A2605 (2015).
2. W. Li, E. M. Erickson, and A. Manthiram, *Nat. Energy*, **5**, 26 (2020).
3. R. Schmuch, R. Wagner, G. Hörpel, T. Placke, and M. Winter, *Nat. Energy*, **3**, 267 (2018).
4. D. Andre, S.-J. Kim, P. Lamp, S. F. Lux, F. Maglia, O. Paschos, and B. Stiaszny, *J. Mater. Chem. A*, **3**, 6709 (2015).
5. S.-T. Myung, F. Maglia, K.-J. Park, C. S. Yoon, P. Lamp, S.-J. Kim, and Y.-K. Sun, *ACS Energy Lett.*, **2**, 196 (2017).
6. H.-J. Noh, S. Youn, C. S. Yoon, and Y.-K. Sun, *J. Power Sources*, **233**, 121 (2013).
7. U. H. Kim et al., *Energy Environ. Sci.*, **11**, 1271 (2018).
8. J. Li and A. Manthiram, *Adv. Energy Mater.*, **9**, 1902731 (2019).
9. C. S. Yoon, H.-H. Ryu, G.-T. Park, J.-H. Kim, K.-H. Kim, and Y.-K. Sun, *J. Mater. Chem. A*, **6**, 4126 (2018).
10. J.-H. Kim, H.-H. Ryu, S. J. Kim, C. S. Yoon, and Y.-K. Sun, *ACS Appl. Mater. Interfaces*, **11**, 30936 (2019).
11. Q. Xie and A. Manthiram, *Chem. Mater.*, **32**, 7413 (2020).
12. Y. Kim, *ACS Appl. Mater. Interfaces*, **4**, 2329 (2012).
13. J. Li, A. R. Cameron, H. Li, S. Glazier, D. Xiong, M. Chatzidakis, J. Allen, G. A. Botton, and J. R. Dahn, *J. Electrochem. Soc.*, **164**, A1534 (2017).
14. J. E. Harlow et al., *J. Electrochem. Soc.*, **166**, A3031 (2019).
15. Y.-K. Sun, S.-T. Myung, B.-C. Park, J. Prakash, I. Belharouak, and K. Amine, *Nat. Mater.*, **8**, 320 (2009).
16. J. Langdon and A. Manthiram, *Energy Storage Mater.*, **37**, 143 (2021).
17. R. Jung, M. Metzger, F. Maglia, C. Stinner, and H. A. Gasteiger, *The Journal of Physical Chemistry Letters*, **8**, 4820 (2017).
18. R. Jung, M. Metzger, F. Maglia, C. Stinner, and H. A. Gasteiger, *J. Electrochem. Soc.*, **164**, A1361 (2017).
19. J. Wandt, A. T. S. Freiberg, A. Ogrodnik, and H. A. Gasteiger, *Mater. Today*, **21**, 825 (2018).
20. D. Streich, C. Erk, A. Guéguen, P. Müller, F.-F. Chesneau, and E. J. Berg, *The Journal of Physical Chemistry C*, **121**, 13481 (2017).
21. L. Giordano, P. Karayaylali, Y. Yu, Y. Katayama, F. Maglia, S. Lux, and Y. Shao-Horn, *The Journal of Physical Chemistry Letters*, **8**, 3881 (2017).
22. A. T. S. Freiberg, M. K. Roos, J. Wandt, R. de Vivie-Riedle, and H. A. Gasteiger, *The Journal of Physical Chemistry A*, **122**, 8828 (2018).
23. D. P. Abraham, R. D. Twesten, M. Balasubramanian, I. Petrov, J. McBreen, and K. Amine, *Electrochem. Commun.*, **4**, 620 (2002).
24. S. Venkatraman and A. Manthiram, *Chem. Mater.*, **15**, 5003 (2003).
25. F. Friedrich, B. Strehle, A. T. S. Freiberg, K. Kleiner, S. J. Day, C. Erk, M. Piana, and H. A. Gasteiger, *J. Electrochem. Soc.*, **166**, A3760 (2019).
26. B. Strehle, F. Friedrich, and H. A. Gasteiger, *J. Electrochem. Soc.*, **168**, 050512 (2021).
27. S. Solchenbach, G. Hong, A. T. S. Freiberg, R. Jung, and H. A. Gasteiger, *J. Electrochem. Soc.*, **165**, A3304 (2018).
28. J. Wandt, A. Freiberg, R. Thomas, Y. Gorlin, A. Siebel, R. Jung, H. A. Gasteiger, and M. Tromp, *J. Mater. Chem. A*, **4**, 18300 (2016).
29. R. Jung, F. Linsenmann, R. Thomas, J. Wandt, S. Solchenbach, F. Maglia, C. Stinner, M. Tromp, and H. A. Gasteiger, *J. Electrochem. Soc.*, **166**, A378 (2019).
30. Z. Ruff, C. Xu, and C. P. Grey, *J. Electrochem. Soc.*, **168**, 060518 (2021).
31. L. M. Thompson, J. E. Harlow, A. Eldesoky, M. K. G. Bauer, J. H. Cheng, W. S. Stone, T. Taskovic, C. R. M. McFarlane, and J. R. Dahn, *J. Electrochem. Soc.*, **168**, 020532 (2021).
32. L. de Biasi, A. O. Kondrakov, H. Geßwein, T. Brezesinski, P. Hartmann, and J. Janek, *The Journal of Physical Chemistry C*, **121**, 26163 (2017).
33. A. O. Kondrakov, A. Schmidt, J. Xu, H. Geßwein, R. Mönig, P. Hartmann, H. Sommer, T. Brezesinski, and J. Janek, *The Journal of Physical Chemistry C*, **121**, 3286 (2017).
34. S. Oswald, D. Pritzl, M. Wetjen, and H. A. Gasteiger, *J. Electrochem. Soc.*, **167**, 100511 (2020).
35. S. Oswald, M. Bock, and H. A. Gasteiger, *J. Electrochem. Soc.*, **169**, 050501 (2022).
36. S. Oswald, D. Pritzl, M. Wetjen, and H. A. Gasteiger, *J. Electrochem. Soc.*, **168**, 120501 (2021).
37. S. Oswald, M. Bock, and H. A. Gasteiger, *manuscript in preparation*.
38. L. de Biasi, B. Schwarz, T. Brezesinski, P. Hartmann, J. Janek, and H. Ehrenberg, *Adv. Mater.*, **31**, 1900985 (2019).
39. S. Watanabe, M. Kinoshita, T. Hosokawa, K. Morigaki, and K. Nakura, *J. Power Sources*, **258**, 210 (2014).
40. H.-H. Sun and A. Manthiram, *Chem. Mater.*, **29**, 8486 (2017).
41. J.-H. Kim, S. J. Kim, T. Yuk, J. Kim, C. S. Yoon, and Y.-K. Sun, *ACS Energy Lett.*, **3**, 3002 (2018).
42. E. Trevisanello, R. Ruess, G. Conforto, F. H. Richter, and J. Janek, *Adv. Energy Mater.*, **11**, 2003400 (2021).
43. S. Solchenbach, D. Pritzl, E. J. Y. Kong, J. Landesfeind, and H. A. Gasteiger, *J. Electrochem. Soc.*, **163**, A2265 (2016).
44. S. Solchenbach, *PhD Thesis*, Technical University of Munich (2018).
45. J. Landesfeind, J. Hattendorff, A. Ehrl, W. A. Wall, and H. A. Gasteiger, *J. Electrochem. Soc.*, **163**, A1373 (2016).
46. J. Landesfeind, D. Pritzl, and H. A. Gasteiger, *J. Electrochem. Soc.*, **164**, A1773 (2017).
47. R. Morasch, B. Suthar, and H. A. Gasteiger, *J. Electrochem. Soc.*, **167**, 100540 (2020).
48. S. Drvarič Talian, J. Bobnar, A. R. Sinigoj, I. Humar, and M. Gaberšček, *The Journal of Physical Chemistry C*, **123**, 27997 (2019).
49. K. N. Wood, E. Kazyak, A. F. Chadwick, K.-H. Chen, J.-G. Zhang, K. Thornton, and N. P. Dasgupta, *ACS Central Science*, **2**, 790 (2016).
50. J. Wandt, C. Marino, H. A. Gasteiger, P. Jakes, R.-A. Eichel, and J. Granwehr, *Energy Environ. Sci.*, **8**, 1358 (2015).
51. R. Weber, J.-H. Cheng, A. J. Louli, M. Coon, S. Hy, and J. R. Dahn, *J. Electrochem. Soc.*, **166**, A3250 (2019).
52. G. Bieker, M. Winter, and P. Bieker, *Phys. Chem. Chem. Phys.*, **17**, 8670 (2015).
53. L. Yang, C. Smith, C. Patrissi, C. R. Schumacher, and B. L. Lucht, *J. Power Sources*, **185**, 1359 (2008).
54. G. J. Brug, A. L. G. van den Eeden, M. Sluyters-Rehbach, and J. H. Sluyters, *J. Electroanal. Chem. Interfacial Electrochem.*, **176**, 275 (1984).
55. D. Pritzl, J. Landesfeind, S. Solchenbach, and H. A. Gasteiger, *J. Electrochem. Soc.*, **165**, A2145 (2018).
56. D. T. Boyle, W. Huang, H. Wang, Y. Li, H. Chen, Z. Yu, W. Zhang, Z. Bao, and Y. Cui, *Nat. Energy*, **6**, 487 (2021).
57. H.-H. Ryu, G.-T. Park, C. S. Yoon, and Y.-K. Sun, *Small*, **14**, 1803179 (2018).
58. R. Sim, S. Lee, W. Li, and A. Manthiram, *ACS Appl. Mater. Interfaces*, **13**, 42898 (2021).
59. J. Chmiola, G. Yushin, Y. Gogotsi, C. Portet, P. Simon, and P. L. Taberna, *Science*, **313**, 1760 (2006).
60. W. Li, H. Y. Asl, Q. Xie, and A. Manthiram, *JACS*, **141**, 5097 (2019).
61. I. Hamam, N. Zhang, A. Liu, M. B. Johnson, and J. R. Dahn, *J. Electrochem. Soc.*, **167**, 130521 (2020).
62. D. Pritzl, T. Teufl, A. T. S. Freiberg, B. Strehle, J. Sicklinger, H. Sommer, P. Hartmann, and H. A. Gasteiger, *J. Electrochem. Soc.*, **166**, A4056 (2019).
63. I. A. Shkrob, J. A. Gilbert, P. J. Phillips, R. Klie, R. T. Haasch, J. Bareño, and D. P. Abraham, *J. Electrochem. Soc.*, **164**, A1489 (2017).
64. J. Sicklinger, M. Metzger, H. Beyer, D. Pritzl, and H. A. Gasteiger, *J. Electrochem. Soc.*, **166**, A2322 (2019).
65. R. Jung, R. Morasch, P. Karayaylali, K. Phillips, F. Maglia, C. Stinner, Y. Shao-Horn, and H. A. Gasteiger, *J. Electrochem. Soc.*, **165**, A132 (2018).
66. Z. Chen, J. Wang, J. Huang, T. Fu, G. Sun, S. Lai, R. Zhou, K. Li, and J. Zhao, *J. Power Sources*, **363**, 168 (2017).
67. J. Langdon and A. Manthiram, *Adv. Funct. Mater.*, **31**, 2010267 (2021).
68. B. Strehle, S. Solchenbach, M. Metzger, K. U. Schwenke, and H. A. Gasteiger, *J. Electrochem. Soc.*, **164**, A2513 (2017).
69. A. T. S. Freiberg, J. Sicklinger, S. Solchenbach, and H. A. Gasteiger, *Electrochim. Acta*, **346**, 136271 (2020).
70. F. Riewald, P. Kurzhals, M. Bianchini, H. Sommer, J. Janek, and H. A. Gasteiger, *J. Electrochem. Soc.*, **169**, 020529 (2022).
71. U. Kasavajjula, C. Wang, and A. J. Appleby, *J. Power Sources*, **163**, 1003 (2007).
72. M. Wetjen, D. Pritzl, R. Jung, S. Solchenbach, R. Ghadimi, and H. A. Gasteiger, *J. Electrochem. Soc.*, **164**, A2840 (2017).